Journal of Manufacturing Processes 114 (2024) 232–246

Contents lists available at ScienceDirect

Journal of Manufacturing Processes

journal homepage: www.elsevier.com/locate/manpro

Numerical studies on cold spray gas dynamics and powder flow in circular and rectangular nozzles

Theodore Gabor [a], Semih Akin [b], Martin Byung-Guk Jun [a,*]

[a] School of Mechanical Engineering, Purdue University, 585 Purdue Mall, West Lafayette 47907, IN, USA
[b] Department of Mechanical, Aerospace and Nuclear Engineering, Rensselaer Polytechnic Institute, Troy, NY 12180, USA

ARTICLE INFO

Keywords:
Cold spray
Supersonic nozzle
Rectangular nozzle
Numerical modeling
CFD
Additive manufacturing
Composite metallization

ABSTRACT

Cold Spray (CS) is an emerging metal additive manufacturing and surface coating technology, where metallic microscale powders are accelerated to supersonic velocities followed by impact onto a target substrate. In CS, the design of the cold spray nozzle is the pillar, determining the efficacy and quality of the deposited layers as it both affects the gas dynamics and powder flow. However, comparative studies on the gas-powder flow dynamics within different nozzle profiles are limited. In this paper, two prominent CS nozzle exit profiles – circular and rectangular – are extensively studied using numerical modeling by considering both soft and hard feedstock powders (i.e., tin (Sn) and copper (Cu)). In this regard, computational fluid dynamics (CFD) simulations are performed to investigate the effect of inlet gas pressure and temperature on supersonic jet formation and powder dispersion characteristics. In regard to the gas flow, the rectangular nozzle showed flow separation much earlier in the nozzle compared to the circular nozzle under the same process settings. Notably, this phenomenon was found to be more drastic at lower gas pressures. As for the powder flow, it was observed that the rectangular nozzle is less effective at accelerating powders compared to the circular nozzle but allows for powders to reach higher temperatures. Moreover, particle deposition experiments on a composite substrate (GFRP) revealed that while the rectangular nozzle produced more uniform particle deposition (R_a = 8.12), it led to a thinner metal coating (≈53 %) with significantly higher electrical resistance (143-fold) compared to the circular nozzle. The results provide valuable insights into understanding the advantages and limitations of both the circular and rectangular nozzle profiles in CS, contributing to more efficient and high-quality particle deposition.

1. Introduction

Cold Spray (CS) – initially developed in the 1980s [1] – is an emerging surface deposition and additive manufacturing (AM) technology, enabling rapid, scalable, and high-throughput fabrication of functional parts and coatings [2–4]. Metallic microscale powders such as aluminum, tin, and copper [3] are accelerated to above the critical velocity using compressed gasses (e, g., air, helium, nitrogen) [2]. The critical velocity is required for the powders to have a high enough energy for consolidation onto the substrate via powder-substrate metallurgical bonding and/or mechanical interlocking processes [4]. Critical velocity is dependent on the material properties of both the feedstock powders and the substrates. Although the substrates are usually metallic [3], other types of substrates including ceramics, polymers, and composites can be also employed in CS [5]. Owing to its low-process temperature, CS has attracted attention in repairing damaged parts and depositing oxygen-sensitive materials [3,6,7] since the bonding mechanism is not reliant on applying extremely high heat or direct energy sources to melt the powders and substrate, which is common in many laser-based AM processes. The low process temperature of the CS also allows for functional surface metallization on low-thermal budget substrates such as polymers [8–10], whereas conventional thermal spray processes operate at temperatures (>1000 °C) [11], thereby limiting their utilization for these important materials. This critical feature of the CS enables the deposition of metal powders onto polymer substrates, allowing for functional surface metallization on polymeric substrates [8,9,12,13]. Particularly, electrically conductive metallization on composite materials using CS has garnered great attention in the domain of lightning strike protection [14]. Furthermore, CS has been used for the rapid deposition of oxygen-sensitive materials on oxygen-sensitive substrates [15] for corrosion-resistant coatings [16]. Taken all together, the CS process has been shown to be a green process as it does not require any high-temperature, vacuum chamber, strong chemicals,

* Corresponding author.
E-mail address: mbgjun@purdue.edu (M.B.-G. Jun).

https://doi.org/10.1016/j.jmapro.2024.02.005
Received 4 October 2023; Received in revised form 24 January 2024; Accepted 3 February 2024
Available online 13 February 2024
1526-6125/© 2024 The Society of Manufacturing Engineers. Published by Elsevier Ltd. All rights reserved.

Nomenclature

Symbol

A_p	Particle cross sectional area (m^2)
A_{sp}	Particle surface area (m^2)
a	Experimental parameters for Drag Coefficient
C_D	Drag Coefficient
C_p	Specific heat of air (1006.43 $J.(kgK)^{-1}$)
C_{part}	Specific heat of the particles (381 $J.kg^{-1}.K^{-1}$ for Cu and 221.89 $J.kg^{-1}.K^{-1}$ for Sn)
d	Particle diameter (μm)
$\overline{d}$	Average particle diameter (μm)
d_{50}	Median particle diameter (μm)
F_i, $\vec{F}$	Force (N)
$\vec{g}$	Acceleration of gravity ($m.s^{-2}$)
h	Particle convection coefficient
k_T	Thermal conductivity of air (0.0242 $W.(mK)^{-1}$).
L	Length (m)
m	Mass of air (kg)
m_p	Particle mass (kg)
$\dot{m}_p$	Particle mass flow rate ($kg.s^{-1}$)
M_p	Particle Mach number
n	Rosin-Rammler diameter distribution parameter
Nu_p	Particle Nusselt Number
P	Pressure (MPa)
Pr	Prandtl Number
R	Ideal gas constant (8.314 $J.K^{-1}.mol^{-1}$), line resistance (Ω)
R_a	Average surface roughness (μm)
Re	Gas Reynold's Number
Re_p	Particle Reynold's Number
S	Separation distance of DDA
t	Time (s), layer thickness of an electrode
T	Temperature (K, °C)
T_{outlet}	Measured nozzle outlet temperature (°C)
T_p	Particle temperature (K, °C)
T_r	Recovery temperature (K, °C)
u, v, w	Cartesian velocity components ($m.s^{-1}$)
w	Width (m)
V	Volume of gas (m^3)
$\vec{v}$	Gas velocity vector ($m.s^{-1}$)
$\vec{v_p}$	Particle velocity vector ($m.s^{-1}$)
x, y, z	Cartesian positional components (m)
μ	Viscosity of air (1.789×10^{-5} kg. $(ms)^{-1}$)
ρ	Density of air ($kg.m^{-3}$), electrical resistivity (Ω.m)
ρ_p	Particle material density ($kg.m^{-3}$)
φ	Angle between dual deposited material and notch location of the DDA (degrees)
ω	Angular velocity of the DDA (RPM)
Ω	Ohm (unit of electrical resistance)

Abbreviation

AM	Additive Manufacturing
CD	Converging-Diverging
CFD	Computational Fluid Dynamics
CFRP	Carbon Fiber Reinforced Polymer
CS	Cold Spray
Cu	Copper
DDA	Dual Disk Anemometer
ER	Expansion Ratio
GFRP	Glass Fiber Reinforced Polymer
IR	Infrared
LPCS	Low Pressure Cold Spray
RANS	Reynolds Averaged Navier Stokes
RT	Room Temperature
SEM	Scanning Electron Microscopy
Sn	Tin

plasma, or precursors [10,16].

In CS, the deposition efficacy and quality strictly depend on the particles' impact velocity. Herein, the supersonic nozzle - also known as converging-diverging (CD) nozzle or de Laval nozzle- is the backbone of the CS process to accelerate particles above the critical velocity for achieving particle deposition on the target surface. Furthermore, deposition resolution and shape of the spray spot size greatly depend on the geometry of the nozzle's divergent section and exit profile [17]. Particularly, the exit profile of the nozzle determines the quality, uniformity, and precision of the resulting deposition. As such, the design of the supersonic nozzle is critically important to achieve the desired surface deposition via the CS process.

Given that nozzle design greatly affects the powder deposition characteristics in CS, many attempts have been made to understand how the gas-particle flow is affected by nozzle geometry. There are mainly two nozzle configurations used in CS, namely: i) axisymmetric; and ii) non-axisymmetric. The majority of CS nozzles incorporate an axisymmetric profile such as a circular profile, which has been known for decades to accelerate the driving gas above supersonic velocities (i.e., Mach >1) [18]. Among the axisymmetric nozzles, there are nozzle profiles such as the conical convergent-divergent, the bell convergent-divergent, the convergent-barrel, and the convergent-divergent-barrel nozzle [19]. The conical convergent-divergent nozzle - also simply known as circular nozzle - has been the most common and extensively studied nozzle design in the literature. Suo et al. [20] studied the effects of changing critical nozzle dimensions such as nozzle expansion ratio (ER) (i.e., the ratio of the areas of nozzle exit to throat), showing that the nozzle expansion ratio remarkably influences the gas and powder velocities. Cao et al. [21,22] studied the effects of inlet diameter, convergent length, divergent length, and expansion ratio, where it was shown that increasing inlet diameter and convergent length raised particle temperature and velocity before the nozzle throat. Additionally, increasing the divergent length and expansion ratio increased particle velocity and temperature, but only to a point where a maximum particle velocity is reached. In Ref [21], optimization methods were also explored by considering particle density and size. Akin et al. [23] investigated the nozzle expansion ratio for nanoparticle-filled droplets and reported that the optimal expansion ratio of a circular nozzle is around 1.5–2.0 for low-inertia liquid droplets compared to the suggested range of 5–9 for metal particles.

Some studies investigated the effects of changing the powder injection location within the nozzle in the direction of the nozzle's central axis [24,25]. In these studies, it was shown that injecting the powder at the convergent section resulted in an increased powder spread, whereas injecting the powders at the throat reduced the powder dispersion. Additionally, the configurations where the powders are injected into the throat are affected more by powder preheating [25]. Injecting powders in an off-axis direction at or after the nozzle throat was studied by Huang et al. [26], and it was shown that this configuration results in more powder-wall interactions which can cause particle spreading, increasing the nozzle wear over time. Moreover, explorations of particle deposition on non-flat target surfaces using a circular nozzle have been examined by numerical modeling to predict the deposition morphology and particle dispersion [27,28]. More recently, the bell-shaped converging-diverging nozzles have been explored in CS [29] and it was shown that a bell-shaped divergent section accelerates the gas and powder more

quickly, allowing for a reduced nozzle length. Additionally, Zavalan and Rona [19] provided a method to optimize the shape of the divergent bell in bell-type nozzles. In this case, the optimized bell shape design created a more dispersed but even powder stream with higher powder velocities compared to the conical nozzle. However, it remains challenging to pragmatically employ bell-type nozzles in CS due to their manufacturing difficulties raised by geometrical complexity.

Although the circular profile is the most common in CS, non-axisymmetric nozzles such as rectangular nozzle profile have been employed to create wide particle deposition tracks [30]. In CS, a wider deposition track allows for a reduction in the number of passes needed to coat a surface, thereby shortening the processing time. In addition, the authors of the present study also showed that rectangular nozzles produce a more even deposition profile compared to circular nozzles [31]. Yin et al. [32] showed that rectangular nozzles generate a higher average particle velocity as compared to elliptical nozzle profiles of the same width/length ratio, which reduces the bow shock that inherently appears on the substrate. Some studies reported that the bow shock does reduce the particle impact velocity [33,34], so implementing methods to reduce the strength of the bow shock is valuable for the CS process. However, width/length ratios <0.2 drastically reduce particle velocity even if the bow shock wave is also weak [32]. Further investigation on the rectangular nozzle profile by Varadaraajan and Mohanty [35] by incorporating a radial powder injector showed that although the radial powder feed angle did not affect particle velocity, it influences particle dispersion. In addition, the expansion ratio was also investigated in the same study [35], showing that slightly over-expanded flows produced the highest particle velocities compared to under-expanded flows for the rectangular nozzle. Despite these works, along with significant advances in nozzle design for CS, comparative studies on the effects of different nozzle profiles (i.e., axisymmetric, non-axisymmetric) on cold spray gas dynamics and powder dispersion are limited. As such, there remains a critical need for a study that comprehensively investigates and compares the axisymmetric (circular) and non-axisymmetric (rectangular nozzle) geometries to uncover the flow structure and powder behavior in the nozzles under an inclusive set of CS process conditions.

To this end, the present study aims to fill this critical gap by comparatively investigating the gas dynamics-powder flow relationships considering both circular and rectangular nozzle profiles. The primary objective of this study is to elucidate the combined effects of nozzle profiles and driving gas conditions (i.e., pressure, temperature) on flow structure and particles in-flight and upon-impact behaviors. In this regard, numerical modeling studies through computational fluid dynamics (CFD) simulations are conducted using discrete phase modeling through the Eulerian-Lagrangian scheme. The numerical modeling results are then justified and validated based on particles impact velocity as well as gas inlet/outlet stagnation temperature analyses. Afterwards, a comprehensive examination of gas-powder flow and powder deposition spread for both circular and rectangular nozzles is performed by employing both soft (tin) and hard (copper) feedstock powders. Three key process parameters, namely inlet pressure, inlet temperature, and powder material, are considered to understand their effects on gas-powder flow structure and particle deposition. Lastly, an experimental case study on CS is conducted to characterize and compare the resulting depositions in terms of layer thickness, surface roughness, electrical conductivity, and microstructure for both nozzle types. The main contribution of this work pertains to providing valuable insights into the advantages and limitations of circular and rectangular nozzle profiles in the CS process. These insights highlight potential areas for nozzle design improvements to achieve more effective and precise particle deposition.

2. Materials and methodology

2.1. Materials

Fig. 1a–b shows the morphology and size distribution of the copper (Cu) and tin (Sn) feedstock material (*Centerline Inc.*) considered in the numerical and experimental studies. The Cu particles have a spherical shape with a size range of 5–44 μm, and the median particle diameter (d_{50}) is ≅36 μm. In addition, the Sn particles have a quasi-spherical shape with a size range of 5–44 μm, where the $d_{50} \cong 17$ μm. Fig. 1c demonstrates both rectangular and axisymmetric nozzle configurations used in numerical modeling and experimental studies. The important dimensions of both nozzles are also presented in Fig. 1d. The glass fiber-reinforced polymer (GFRP) plates (*Bond Laminates, Germany*) having a thickness of 1 mm were used as the target substrate in experimental deposition studies.

A low-pressure CS system (*Rus Sonic Technology, Inc.*) was employed in the deposition experiments using compressed air as the driving gas. In the experiment studies, the spray distance and the nozzle speed were set to 30 mm and 50 mm/s, respectively. The temperature profile of the nozzles was obtained by an infrared (IR) thermal camera (*FLIR A300, FLIR Systems*), while the gas temperature was measured using a type-K thermocouple *(Hanna Instruments)*. The electrical resistance of the deposited metal layers was measured by a digital multimeter (*Agilent 34401A*). Moreover, layer thickness and surface roughness were obtained via a digital micrometer (*REXBETI*) and surface roughness tester (*AMTAST*), respectively. Lastly, scanning electron microscopy (SEM) was performed to analyze the microstructural morphology.

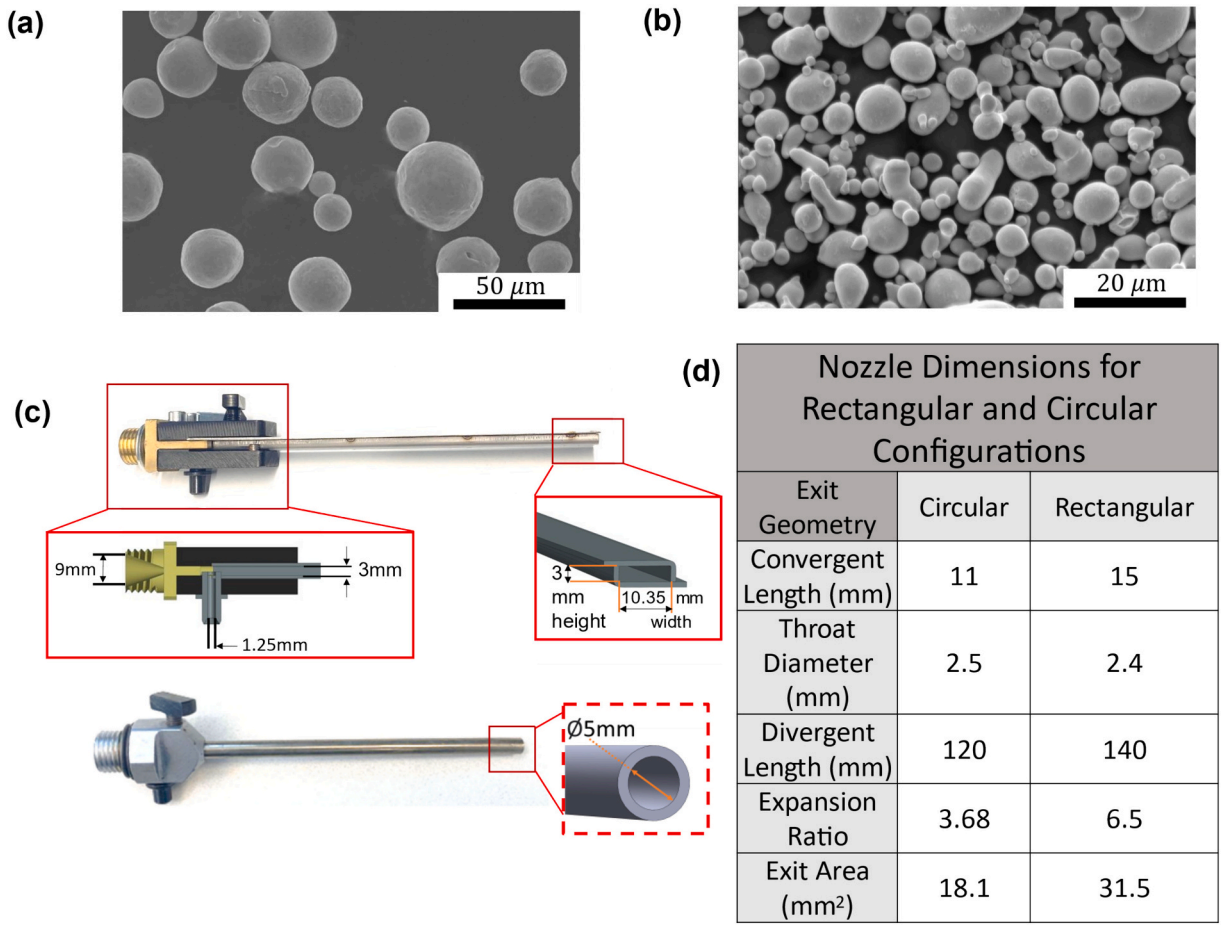
2.2. Methodology (numerical modeling)

In this section, the numerical modeling approach is discussed, in which three-dimensional (3-D) gas-powder flow is modeled via a Eulerian-Lagrangian approach. First, the 3D flow domain is introduced, covering boundary conditions and grid discretization for both nozzle types. Afterwards, the gas phase flow is comprehensively examined, encompassing geometrical effects such as nozzle expansion ratio as well as flow effects like turbulence and heat transfer within the gas flow. Lastly, the Lagrangian powder phase is discussed, which includes the powder force equations, the contribution of turbulence, and the gas-particle heat transfer equations.

2.2.1. Flow domain

In regard to modeling of cold spray gas dynamics and powder dispersion, the majority of research performed involves numerical modeling in either a 2D-Axisymmetric or 3D scheme. Unlike 1D Isentropic models, 2-D and 3-D numerical modeling can more easily account for changes in ambient pressure, fluid viscosity, flow outside the supersonic jet, boundary layers, and turbulence [36]. To consider the turbulent flow in CS nozzles, various turbulence models have been used extensively, with a large portion of the modeling involving RANS-based turbulence modeling such as standard, RNG, and realizable k-ε turbulence modeling [36], which are quicker to compute compared to Large Eddy Simulation (LES) and Detached Eddy Simulation models [36,37]. A preliminary examination of different turbulence models by Yin et al. [36] showed that changing the turbulence models affect the predicted shock wave pattern. However, when comparing the SST k-ω model to the LES model, Ozdemir et al. [38] found little difference between the two's impact on particle velocity.

It is important to note that the CS nozzles are inherently non-axisymmetric due to the location of the radial powder inlet port. In addition, a rectangular nozzle flow cannot be accurately captured in a 2D planar model due to the non-uniform length/width ratio of the diverging exit profile. Therefore, a three-dimensional (3D) modeling of the flow domain should be a more appropriate choice over 2D flow domain for numerical modeling of gas-particle flow in CS. In light of the



Nozzle Dimensions for Rectangular and Circular Configurations		
Exit Geometry	Circular	Rectangular
Convergent Length (mm)	11	15
Throat Diameter (mm)	2.5	2.4
Divergent Length (mm)	120	140
Expansion Ratio	3.68	6.5
Exit Area (mm^2)	18.1	31.5

Fig. 1. Morphology of **(a)** Cu **(b)** Sn particles; **(c)** representative images of square nozzle (upper panel) and axisymmetric nozzle (bottom panel); **(e)** important dimensions of the nozzles.

above information, this study employs a 3-D turbulent flow modeling approach using the RANS-based realizable k-ε turbulence model to study the 3-D flow development in rectangular and circular CS nozzle profiles. In this regard, as shown in Fig. 2, 3D flow domain of both the rectangular and circular nozzle profiles are set up using a commercial computational fluid dynamics (CFD) package (ANSYS® Fluent 22.2). In addition to the rectangular nozzles illustrated in Fig. 1–2, an additional rectangular nozzle was simulated, with an expansion ratio (ER) of 3.7 and a divergent length of 120 mm to provide further comparison between rectangular and circular nozzle profiles with identical expansion ratio. The results are discussed in Section 3.

Three inlet and one outlet boundary conditions were set up in numerical modeling studies. The inlet boundary conditions involve the: 1) inlet gas pressure (0.4–0.7 MPa); 2) inlet gas temperature (293–530 K); and 3) powder injection, while the outlet condition was set to atmospheric pressure (1 atm). Compressible air was considered as the driving gas and powder carrier gas. The powder inlet port was set to be atmospheric pressure at room temperature (293 K) with a powder feed rate of 1.5×10^{-4} kg·s^{-1}. The powder injection velocity was set to 10 m/s in the radial direction starting from the powder injection port location. At the downstream flow, a cylinder domain (40 mm × 40 mm) was placed at the nozzle exit to simulate open-air space, with the nozzle exit protruding 5 mm into this section. The cylinder domain was set to the atmospheric pressure at 293 K to improve simulation convergence. The end cap of this cylinder was considered as the target substrate surface, and trapping boundary condition was assigned on the substrate to capture the impact velocity of impinging particles as well as their dispersion (spread) on the target surface. All walls are considered to be made of aluminum to ensure consistency in powder-wall interactions.

2.2.2. Gas phase (continuous phase)

Given the above-mentioned boundary conditions, the continuous gas phase was modeled based on the Eulerian approach. In this regard, the Navier-Stokes equations were solved by considering pressure-based compressible supersonic flow at steady-state conditions. In this case, the density of air (referred to as ρ for all following equations) is determined by the ideal gas law ($PV = \frac{mRT}{M}$), where the molar mass of air is set to 28.966 g·mol^{-1}. Eqs. (1)–(4) show the Cartesian form of the continuity and Navier-Stokes equations used for the simulation of continuous gas phase (air) [39]:

Continuity equation:

$$\frac{\partial \rho}{\partial t} + \frac{\partial(\rho u)}{\partial x} + \frac{\partial(\rho v)}{\partial y} + \frac{\partial(\rho w)}{\partial z} = 0 \tag{1}$$

Momentum equations:

$$\rho F_x - \frac{\partial P}{\partial x} + \mu\left(\frac{\partial^2 u}{\partial x^2} + \frac{\partial^2 u}{\partial y^2} + \frac{\partial^2 u}{\partial z^2}\right) + \frac{1}{3}\mu\frac{\partial}{\partial x}\left(\frac{\partial u}{\partial x} + \frac{\partial v}{\partial y} + \frac{\partial w}{\partial z}\right) = \rho\frac{Du}{Dt} \tag{2}$$

$$\rho F_y - \frac{\partial P}{\partial y} + \mu\left(\frac{\partial^2 v}{\partial x^2} + \frac{\partial^2 v}{\partial y^2} + \frac{\partial^2 v}{\partial z^2}\right) + \frac{1}{3}\mu\frac{\partial}{\partial y}\left(\frac{\partial u}{\partial x} + \frac{\partial v}{\partial y} + \frac{\partial w}{\partial z}\right) = \rho\frac{Dv}{Dt} \tag{3}$$

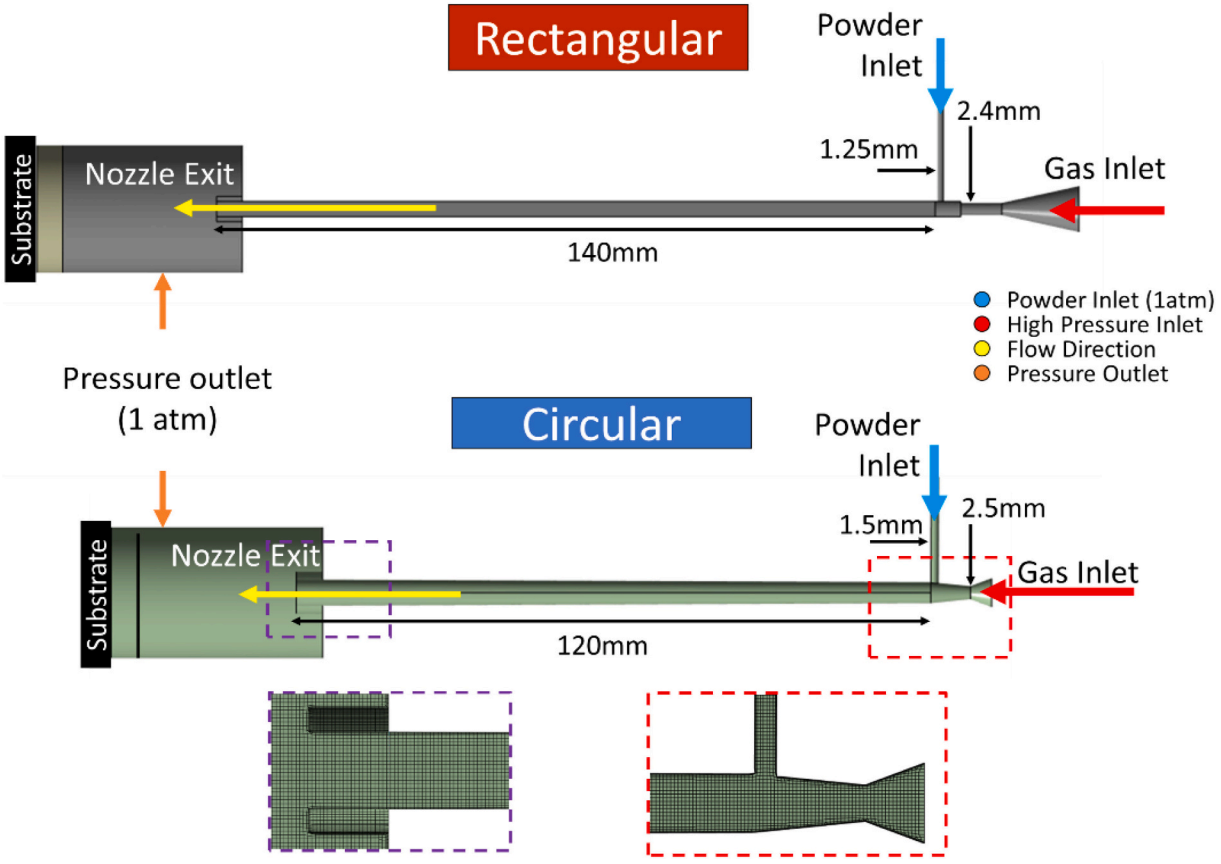


Fig. 2. Computational domain and boundary conditions with meshing cross sections for rectangular (upper panel) and axisymmetric nozzles (bottom panel).

$$\rho F_z - \frac{\partial P}{\partial z} + \mu\left(\frac{\partial^2 w}{\partial x^2} + \frac{\partial^2 w}{\partial y^2} + \frac{\partial^2 w}{\partial z^2}\right) + \frac{1}{3}\mu\frac{\partial}{\partial z}\left(\frac{\partial u}{\partial x} + \frac{\partial v}{\partial y} + \frac{\partial w}{\partial z}\right) = \rho\frac{Dw}{Dt} \tag{4}$$

In these equations, P is the fluid's pressure, μ is the viscosity of air (1.789×10^{-5} kg. (ms)$^{-1}$), and u, v, and w are the fluid velocity components (m·s^{-1}) for coordinate directions x, y, and z (m), respectively. F_i is the force component (N) in the i^{th} direction, and t is time (s). In these equations, the material derivative is denoted as $\frac{D}{Dt} = \frac{\partial}{\partial t} + u\frac{\partial}{\partial x} + v\frac{\partial}{\partial y} + w\frac{\partial}{\partial z}$.

In addition to momentum equations, the conservation of energy equation in Eq. (5) is required to account for the temperature changes of the compressible supersonic jet during CS [39]. In Eq. (5), T (K) is the temperature, C_p is the specific heat of gas (air) (1006.43 J·(kgK)$^{-1}$), and k_T is the thermal conductivity of air (0.0242 W·(mK)$^{-1}$). To account for turbulence effects in the gas flow, the realizable form of the $k-\varepsilon$ turbulence model is used, in which the details can be found in Refs [39, 40].

Energy equation:

$$\frac{\partial}{\partial t}(\rho C_p T) + \frac{\partial(\rho u C_p T)}{\partial x} + \frac{\partial(\rho v C_p T)}{\partial y} + \frac{\partial(\rho w C_p T)}{\partial z} = \frac{\partial}{\partial x}\left(k_T\frac{\partial T}{\partial x}\right) + \frac{\partial}{\partial y}\left(k_T\frac{\partial T}{\partial y}\right) + \frac{\partial}{\partial z}\left(k_T\frac{\partial T}{\partial z}\right) \tag{5}$$

2.2.3. Solid phase (discrete phase)

The discrete powder phase was modeled based on the Lagrangian approach since the volume of powder used is much lower than the volume of gas that flows through the system. The force balance equation for each particle is shown below:

$$m_p\frac{d\vec{v}_p}{dt} = C_D\rho(\vec{v} - \vec{v}_p)|\vec{v} - \vec{v}_p|\frac{A_p}{2} + \frac{\vec{g}(\rho_p - \rho)}{\rho_p} + \vec{F} \tag{6}$$

where m_p, ρ_p, and v_p are the particle mass, velocity, and density, respectively. A_p is the particle's cross-sectional area, which is circular as the particles are assumed to be spherical in nature. In addition, C_D is the particle drag coefficient, and $\vec{F}$ is a lump term referring to any external forces the particle experiences. In this case, turbulent two-way coupling of the gas-particle flow is established to ensure appropriate momentum transfer due to the turbulent flow. As such, the gas-particle interaction forces are defined as:

$$F_p = \sum\left(\frac{18\mu C_D Re}{\rho_p d_p^2 24}(v_p - v) + F_{other}\right)\dot{m}_p\Delta t \tag{7}$$

with $Re = \frac{\rho v L}{\mu}$ is the flow's Reynolds Number with flow dependent characteristic length L; d_p is the particle diameter, $\dot{m}_p$ is the powder mass flow rate, and F_{other} refers to additional forces transferring momentum to the particles. Additionally, a discrete random-walk model was incorporated to further account for turbulent dispersion of the powder flow [39]. As stated before, the powders are assumed to be perfectly spherical, and therefore the Morsi and Alexander drag formulation is used [41]:

$$C_D = a_1 + \frac{a_2}{Re} + \frac{a_3}{Re^2} \tag{8}$$

The constants a_1, a_2 and a_3 based on the flow's Reynolds Number. An additional correction was used to account for flows with particle Mach number $M_p > 0.4$ and $Re_p > 20$ [42]. Particle rotation particle-particle collision and deformation were not considered in the numerical

modeling.

Particle distributions of Cu and Sn are approximated by the Rosin-Rammler model [43], which has been well known to accurately describe powder distributions in CS applications [12,44–46]. For both Sn and Cu, based on the particle distribution data by the vendors (Sn powders from *Centerline Inc.* and Cu from *Chemical Store Inc.*), the maximum powder diameter was set to 44 μm, and the minimum powder diameter was set to 5 μm. Meanwhile, the average powder diameter was specified for each material, with $\overline{d_{Cu}} = 35\ \mu m$ and $\overline{d_{Sn}} = 17\ \mu m$. To properly allocate the diameter distributions among the powders, the Rosin-Rammler distribution equation was used as in Eq. (9), where F_d refers to the mass fraction of the particles greater than a given particle diameter d, and $\overline{d}$ is the average particle diameter stated above. The parameter n (i.e., affects the distribution spread of the diameters) was set to 3.5. In addition, a discrete number of particle diameters must be set for each model; in this case, 10 diameter values were set.

$$F_d = exp\left(- \left(\frac{d}{\overline{d}}\right)^n \right) \tag{9}$$

Heat transfer between the gas and powder phases is performed using the following equation [36]:

$$m_p C_{part} \frac{\partial T_p}{\partial t} = A_{sp} h \left(T_r - T_p\right) \tag{10}$$

In the equation above, C_{part} is the specific heat of the particle phase (381 $J{\cdot}kg^{-1}{\cdot}K^{-1}$ for Cu and 221.89 $J{\cdot}kg^{-1}{\cdot}K^{-1}$ for Sn), and A_{sp} is the surface area of a given particle. T_r and T_p are the recovery and particle temperatures, respectively, and m_p is the particle mass. This formulation is used because for Cold Spray the particle Biot Number is <0.1 [36]. The convection coefficient h is often obtained from the Ranz-Marshal formulation of the particle Nusselt number Nu_p [36], which is described as follows:

$$Nu_p = 2 + 0.6\ Pr^{0.33} Re_p^{0.5} = \frac{hd}{k_t} \tag{11}$$

With Pr being the flow's Prandtl Number, Re_p being the particle reynolds number, d as the particle diameter, and k_t is the thermal conductivity of the gas phase, which is air (0.0242 W. $(mK)^{-1}$).

Lastly, to solve numerical modeling to obtain CFD simulations results, certain assumptions have been made and are summarized as follows:

i. The model was solved under the assumption of pressure-based compressible supersonic flow at steady-state conditions.
ii. The feedstock powders are treated as rigid with perfectly spherical shape.
iii. Interactions between powders such as collision, agglomeration, etc. were neglected.
iv. Possible chemical reactions between the gas and particle phases were neglected.

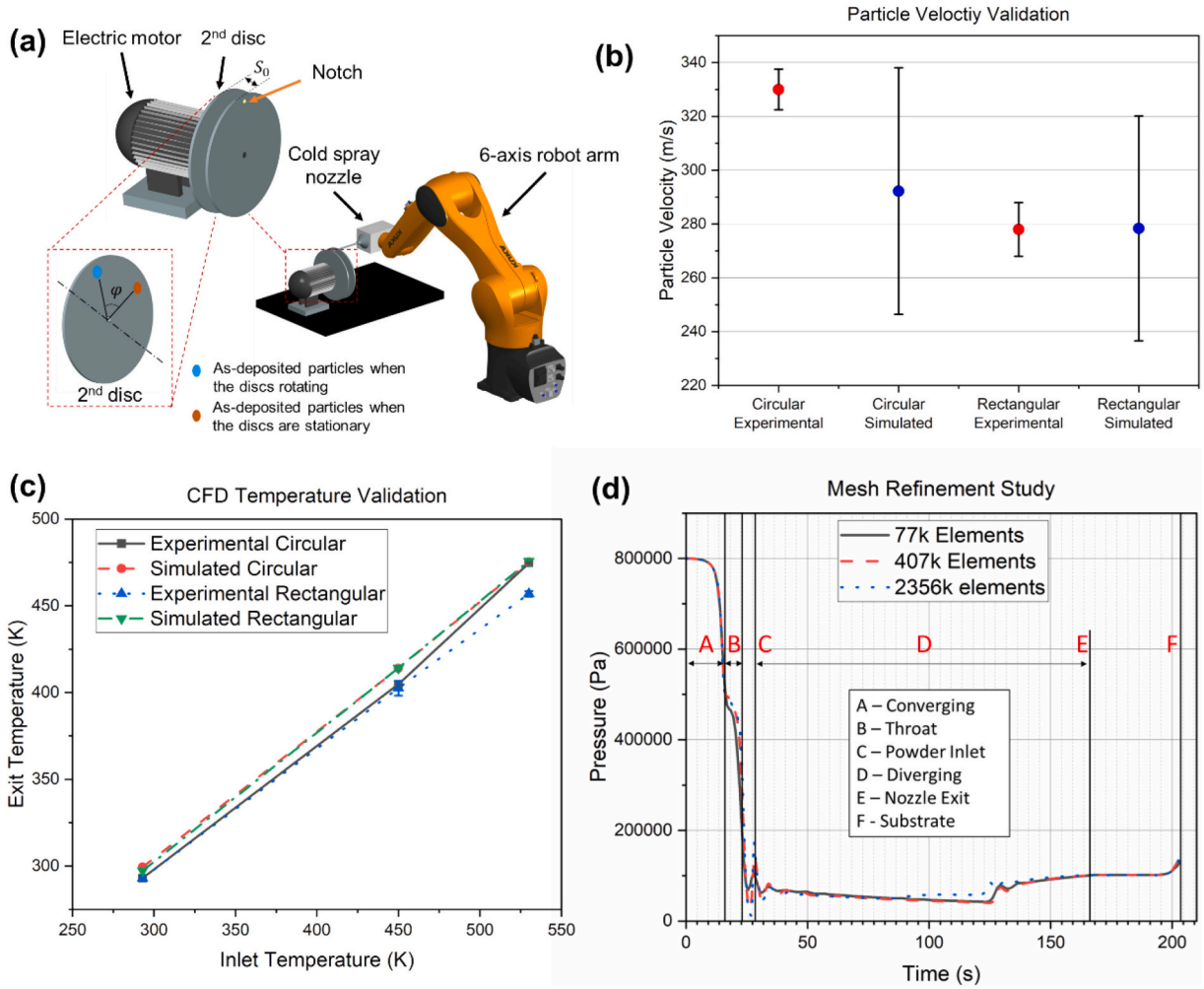


Fig. 3. **(a)** The schematic of the dual disc anemometer (DDA) setup, **(b)** particles impact velocity; **(c)** nozzle inlet/exit temperature results for model validation; **(d)** mesh independency test results.

Acknowledging these assumptions, the numerical model was collectively solved to generate the CFD simulations. The ultimate goal is to understand the gas dynamics and powder dispersion characteristics in different nozzle geometries, such as circular and rectangular nozzles.

3. Results and discussion

3.1. Model validation

The numerical modeling results were justified and verified by considering: i) particles' impact velocity; and ii) driving gas temperature. First, to capture the particles' impact velocity, we utilized a dual disc anemometer (DDA) setup, which is originally used for measuring air-blast solid particles on substrates [47]. As shown in Fig. 3a, the DDA setup consists of a shaft with two rotary discs having a fixed separation distance of 33 mm. While the dual disc system was rotating at a certain speed (i.e., >10,000 rpm), the particles were cold sprayed through a notch on the first disc, which led to a deposition on the second disc (i.e., recording disc). The angle difference between the notch and the resultant deposition on the second disc is measured to calculate the average particle impact velocity using an equation given below [47];

$$V_p(\varphi) = \frac{6\omega S}{\varphi} \tag{12}$$

where V_p (m·s^{-1}) is the average particle impact velocity, S (m) is the distance between the discs, ω (rpm) is the angular velocity of the disc, and φ (degree) is the angle at which the deposits are found on the recording disc [47]. To capture the particles' impact velocity using the setup, a minimum shaft speed of 10,000 rpm was required [48]. Given that information, we measured the shaft speed as 10,630 rpm using a tachometer (*Extech RPM33*) and calculated the average particle impact velocity using the dual disc setup for different nozzle configurations. Further details of the DDA can be found in Ref [48], and Supporting Information of this study (see Fig. S1).

Fig. 3b compares the numerical predicted average particle impact velocity with experimental data obtained from the DDA setup where the inlet pressure is 0.7 MPa. The average impact velocity for the circular nozzle was predicted within an error rate of 11.4 % of the experimental results, whereas the rectangular nozzle's average impact velocity was predicted within an error rate of 1 % of the experimental results. This difference in the error is likely due to the variations in CFD results compared to the data captured in the DDA. In the CFD, slight differences in injection position on the powder inlet surface and powder mass create an array of particle velocities with a much larger range (225–454 m/s for circular and 197–380 m/s for rectangular). This results in a high standard deviation of powder velocities. However, the CFD model cannot determine whether the particles are successfully deposited, whereas the DDA measures the impact velocity of only deposited particles. As such, the DDA setup leads to much smaller standard deviation, which was found to be more prominent in the circular nozzle case. Overall, the CFD simulations predicted the average particle impact velocity within a 12 % error rate as compared to the experimental DDA measurements, which lays within the acceptable error level in such CFD simulations [38].

In addition to particles impact velocity, another important avenue for validation is the driving gas temperature. Although CS does not subject particles to melting temperatures, heated gas is commonly used to improve powder deposition during this process. Therefore, it is important to capture the gas temperature profile to understand the effect of gas temperature within the nozzle. In this regard, the inlet and outlet temperatures for the nozzles obtained from thermocouples (see Fig. S2, Supporting Information) followed by a comparison with the CFD simulation results. In the simulations, the stagnation temperature profile across a line perpendicular to the nozzle's central axis is probed, and then averaged to obtain the average stagnation temperature. Fig. 3c compares the gas temperatures measured for a given inlet temperature. As seen in Fig. 3c, the experimental and numerical modeling results are comparable to each other, having an error of 0.1–4.1 %. The largest difference was observed for the rectangular nozzle at 530 K, where experimental temperatures are 4.1 % lower than the CFD prediction. This is likely due to the construction of the rectangular nozzle, which includes metal "wings" protruding outwards on two sides of the nozzle (see Fig. 1c). These additional metal structures would dissipate heat by behaving such a fin structure, thereby enhancing the heat transfer area, resulting in a lower gas temperature for rectangular-shaped nozzles.

Lastly, as shown in Fig. 3d, a mesh independency study was performed to track the evolution of static pressure along the rectangular nozzle's central axis. When comparing the results between the number of elements, which increase in order of magnitude for each refinement, the pressure profile remains consistent in all zones, confirming the mesh independence of the numerical modeling. Taken together, the results reveal that the constructed 3-D numerical modeling can capture critical features of the CS process for further investigations on the gas-flow structure and powders in-flight and upon-impact behavior for circular and rectangular nozzle profiles.

3.2. Effects of inlet pressure on gas flow

One of the two primary methods to control the powder deposition quality is to change the inlet gas pressure supplied to the nozzle. If a low-pressure cold spray (LPCS) setup is used, the inlet gas pressure is generally <1 MPa [3]. As such, in this study, the inlet pressures tested range from 0.5 to 0.7 MPa, which is a widely used pressure range in many LPCS studies [26,31,48]. In convergent-divergent nozzles, the difference between the inlet pressure and the back pressure (in our case the ambient pressure) greatly affects the shockwave formations within the nozzle and at the nozzle exit [18]. These effects can be clearly seen in Fig. 4, which shows the development of the gas flow velocity with respect to inlet pressure for rectangular and circular nozzle configurations. For the rectangular nozzle, flow separation appears much earlier than the nozzle outlet at all the pressure ranges (0.5–0.7 MPa). This flow separation is still apparent in the rectangular nozzle with a similar expansion ratio to the circular nozzle (~3.7), showing that the lack of radial symmetry in the nozzle creates areas where the flow can more easily separate and create shock waves. Notably, this phenomenon is more prominent at such low pressure of 0.5 MPa, in which the flow separation occurred 70 mm from the nozzle tip in the wider rectangular nozzle, and 83 mm from the nozzle tip in the narrower nozzle. An oblique shock wave formation was observed at the separation point, which is similar to the over-expanded flow case with modest flow separation [42]. This shock wave pattern is due to the non-axisymmetric shape of the nozzle. Conversely, axisymmetric nozzles produce a normal shock wave inside the nozzle if the pressure difference is too small, but the flow is still supersonic [18]. As such, the gas velocity in rectangular nozzle drops steadily to the trans-sonic range ($0.8 < M < 1.2$).

The circular nozzle profile, on the other hand, has supersonic flow throughout the entirety of the nozzle, with significantly less flow separation as the inlet pressure decreases. The nozzle flow shown in Fig. 4 is an overexpanded jet, resulting in a flow separation downstream of the nozzle. Unlike the rectangular nozzle, the exiting jet flow is entirely supersonic up until the target substrate in the circular nozzle case.

This difference in gas flows of both nozzles can be better seen in the particle impact velocity distribution shown in Fig. 5, as well as Figs. S3–4 (Supporting Information). In Fig. 5, the impact velocities of the particles on the substrate are displayed in relation to the nozzle outlet profile, showing how the particles spread based on inlet pressure and exit geometry. When comparing impact velocities of each nozzle profile, it is clear that the circular nozzle has a higher overall particle impact velocity compared to the rectangular nozzle. This was also confirmed in the validation experiments in Fig. 3b. This can be attributed to the development of gas flow in each nozzle, as the circular nozzle

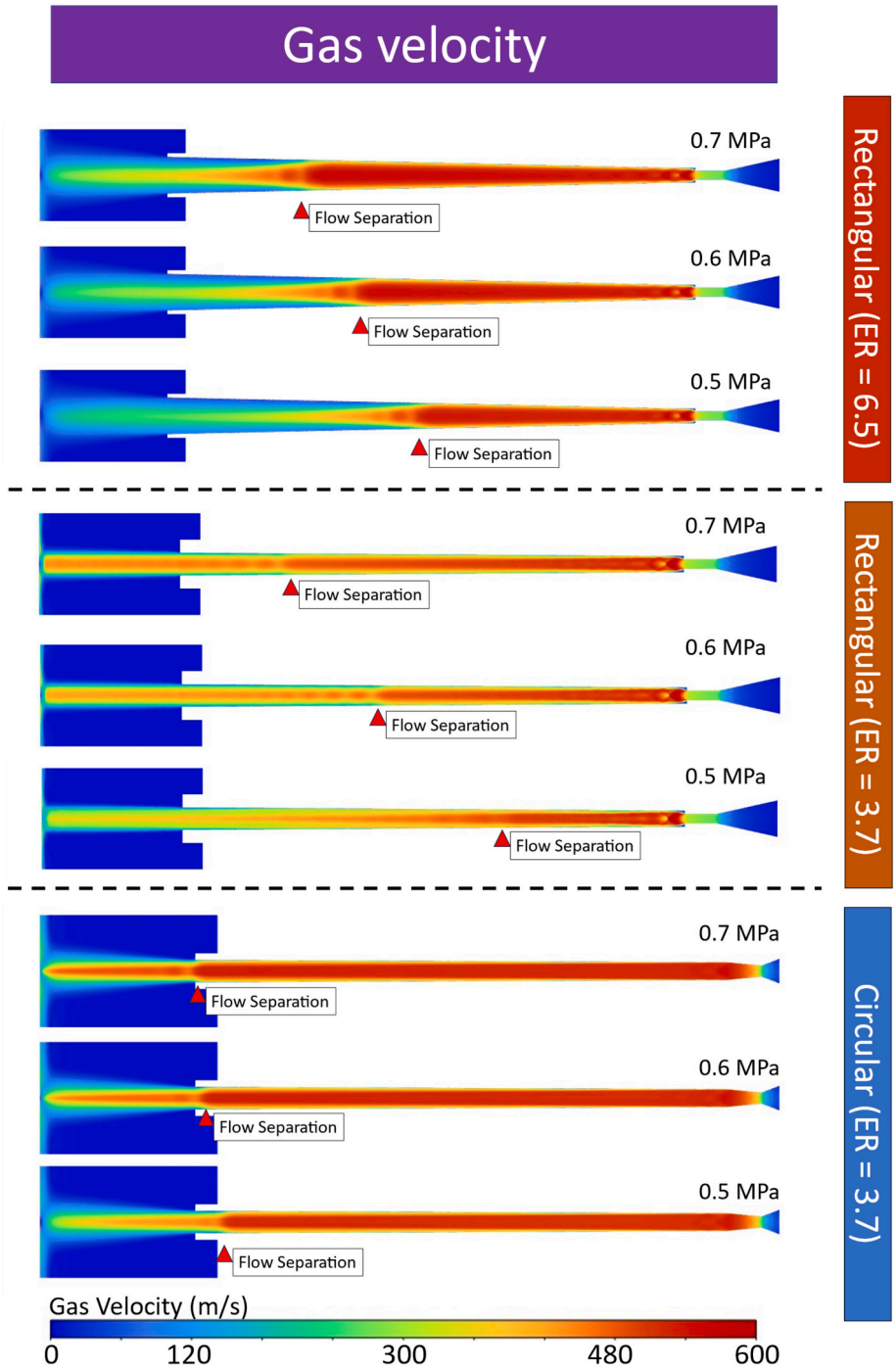


Fig. 4. Contours of the gas velocity at various pressures in rectangular (top panel and middle panels) and circular nozzle (bottom panel).

produced an exiting jet with supersonic gas velocity, whereas the larger rectangular nozzle's exiting jet was in the transonic region. An increase in velocity was observed when reducing the expansion ratio of the rectangular nozzle, which corresponds to the notably supersonic velocity reached from the gas flow in the nozzle. However, it is important to note that both powder and gas velocity values remained lower than what the circular nozzle can produce.

Fig. 5 also shows that the amount of powder spread at the impact region (i.e., substrate surface) is inversely proportional to the inlet pressure, regardless of the nozzle type. For the circular nozzle profile, the $P = 0.5$ MPa case has a slightly larger radius compared to the $P = 0.7$ MPa, having the majority of the impacting powders located within the nozzle's exit profile (which is 5 mm in diameter). This is more substantially seen in the wider rectangular nozzle case as well, where the height of the P = 0.5 MPa deposition profile is ~5 mm larger than the P = 0. 7 MPa case, while the width of the spray pattern is constant. Given that the overall gas velocity is lower at the lower inlet pressures, the powders have more travel time and therefore can rebound between the top and bottom nozzle walls more often. In addition, the initial impact point of the powders in the diverging section gets closer to the powder feed location as pressure decreases, resulting in a higher initial off-axis component in the powder velocity vectors (see Fig. S4). These two factors combined result in a larger powder spread for the rectangular nozzle. In addition, an I-pattern is shown to form in the 0.5 and 0.6 MPa cases, indicating such non-uniform powder spread at these gas pressures. This I-pattern, however, is eliminated in the 0.7 MPa case,

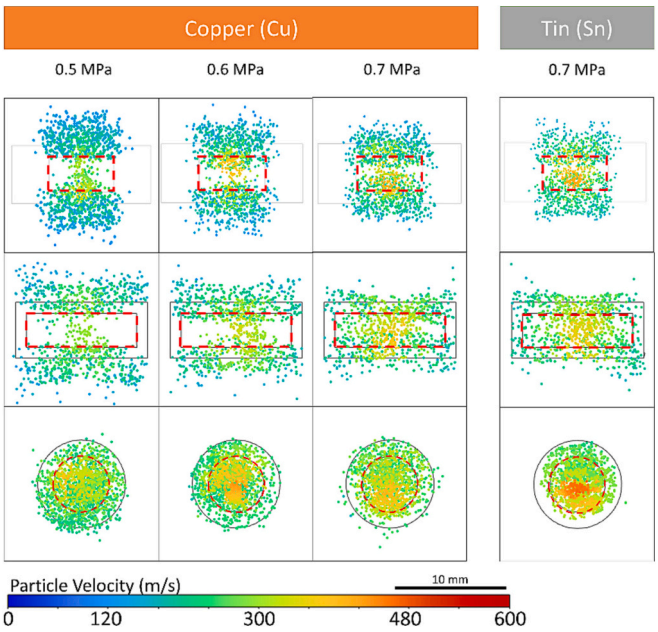


Fig. 5. Effects of gas pressure and powder material on particles impact velocity and dispersion onto the target surface.

meaning that the majority of powders are still within the gas flow jet. A comparable trend can be observed with the narrower rectangular nozzle, but the reduction in height is notably less. This variation is likely attributed to the alteration in nozzle width. Rebounding powders encounter less room to disperse, thus preserving a greater portion of their initial vertical velocity component originating from the initial radial injection point. As such, the importance of a high inlet pressure is highlighted, as a reduction in powder spread ensures that the majority of powders exiting the nozzle impact the substrate at elevated velocity. However, it is also important for rectangular nozzles to be supplied with a high enough inlet pressure to ensure that powders accelerate through a supersonic gas flow for the entirety of the nozzle length as well as a significant portion of the exiting nozzle jet. This is critical to achieve uniform powder dispersion onto the target surface, in which deposition uniformity is a critical aspect in CS applications.

3.3. Effects of powder material

One of the most important parameters that affect the CS process is the powder material, as each material used has a different application for coating and additive manufacturing parts. Furthermore, the critical velocity requirements vary for each powder type used, and therefore it is important to determine how different powder materials travel through and exit the CS nozzle. In this work, hard (Cu) and soft (Sn) feedstock powders were used to understand the gas-powder flow of both material types. As seen in Fig. 5, the lighter and smaller Sn particles reached higher velocities in both the circular and rectangular nozzle profiles, with the more substantial increase shown with the circular nozzle. It is attributed to: i) larger mean particle size of Cu particles (d_{50} = 35 μm) than Sn particles (d_{50} = 17 μm); and ii) greater inertia of Cu particles due to its larger density (8.96 g·cm^{-3}) than Sn particles (7.3 g/cm^{-3}). Taken together, these features led to higher impact velocity for Sn particles as compared to the Cu feedstock for both nozzle profiles.

Additionally, Figs. 5–6 both show a reduction in powder spread for the Sn powders compared to the Cu powders in the circular nozzle profile. When analyzing the powder trajectories of both materials in Fig. 6, the initial impact of the Sn powders in the circular nozzle case is much later in the powders' flight path, resulting in a reduced amount of bouncing between the nozzle walls. As such, the initial off-axis velocity component of the powders was reduced, which affects the nozzle exit trajectory. Lighter powders such as Sn are more likely to be affected by the gas flow as well, which can change their trajectories. However, the internal geometry of the nozzle still does play a role in how the powders impact along the nozzle. This observation is confirmed when examining the impact powder distribution of Cu powders based on powder diameter, which is shown in Fig. S3 (supporting information). Notably, the powders with smaller diameters (and therefore lighter) are focused together and correspond to the higher velocity values in Fig. 5. In contrast, the larger powders exhibit greater dispersion and are more inclined to be located on the edges of the powder distribution profile, correlating with lower powder velocity values.

In the rectangular nozzle cases seen in Figs. 5–6, the powder spread is much tighter (narrower), with the Cu powders having a slightly higher amount of powder spread. This can be attributed to both materials rebounding against nozzle walls at similar locations, as the height of the diverging section's cross-section is much thinner at 3 mm (see Fig. 1c). For the entire diverging section, the cross-section's height of the rectangular nozzle does not increase, as the width of the rectangular section only increases. This is not the case in the circular nozzle, where the powders enter when the nozzle diameter is 4 mm and exit at a nozzle diameter of 5 mm. As such, the rectangular nozzle does not allow for the powders to travel further within the nozzle before losing some kinetic energy due to hitting the nozzle wall. Changing the powder inlet position or implementing a gradual increase in the rectangular nozzle's height may improve the deposition profile and reduce powder spreading while increasing powder velocity.

3.4. Effects of nozzle inlet temperature

Like inlet gas pressure, inlet gas temperature also increases the gas velocity as the average kinetic energy of the gas molecules increases according to the ideal gas law. This, of course, results in an increase in powder velocity, which can be observed when comparing Figs. 5–6 to Fig. 7. In the case of the rectangular nozzle, although the overall powder velocity increases with inlet temperature, Fig. 7a shows that the powder velocity reaches maximum before the nozzle exit. This can be attributed to a similar gas velocity development as shown in Fig. 4, where flow separation occurs inside the diverging section (i.e., 40 mm from the nozzle tip). In addition, the powder velocity is still highest in the center of the rectangular nozzle, resulting in lower powder velocity at the edges of the nozzle wall. Compared to the rectangular nozzle, the majority of the powders in the circular nozzle show a more even velocity development. However, some of the powders do not interact with the nozzle walls, resulting in a large increase in acceleration. This can be better seen in Fig. 7b, where the powders in the bottom half of the nozzle profile have a higher average velocity than the top half portion. In addition, increasing the nozzle inlet temperature significantly increases the overall powder impact velocity.

Moreover, it is important to track the powder temperature development in heated gas flows since the heated gas leads to improved deposition efficiency as the powders' hardness is reduced (i.e., thermal softening) due to the heat transfer between the gas flow and powders [3]. As seen in Fig. S5 (Supporting Information), an increase in nozzle inlet temperature shows an increase in the temperature of the exit jet. Furthermore, as the diverging section expands, gas temperatures rise, allowing for more heat transfer to the injected powders. Fig. 8a shows that the overall particle temperature increases as it travels down the nozzle. Notably, the rectangular nozzle increases the powder temperature to a more significant degree than the circular nozzle for the same inlet temperature. Additionally, the rectangular nozzle's divergent section is 20 mm longer than the circular nozzle's divergent section, which in turn means that the powders will take longer to travel through the nozzle. When considering the lower particle speed of the rectangular nozzle shown in Figs. 5–7, it explains that powders in the rectangular nozzle are exposed to the heated gas flow for much longer than the

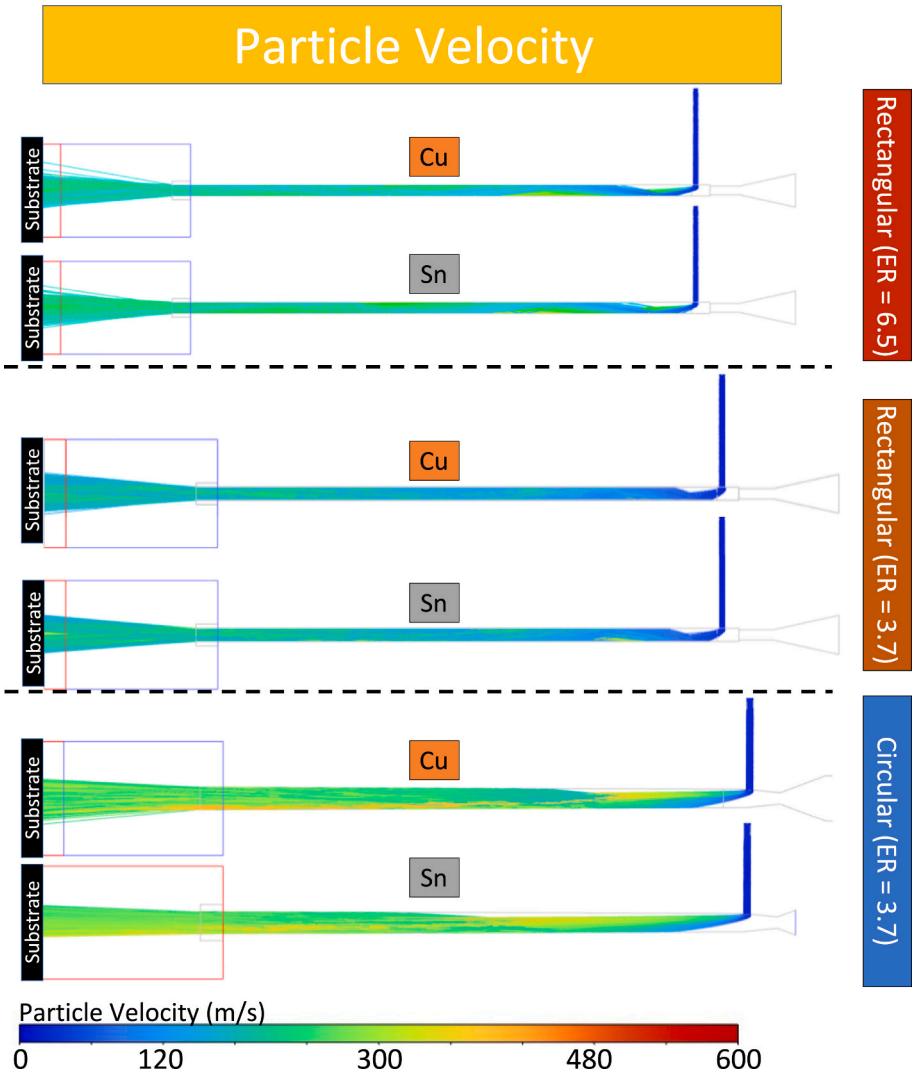


Fig. 6. Particle impact velocity distribution in different nozzle profiles using soft (Sn) and hard (Cu) particles (Inlet gas pressure (P) = 0.7 MPa).

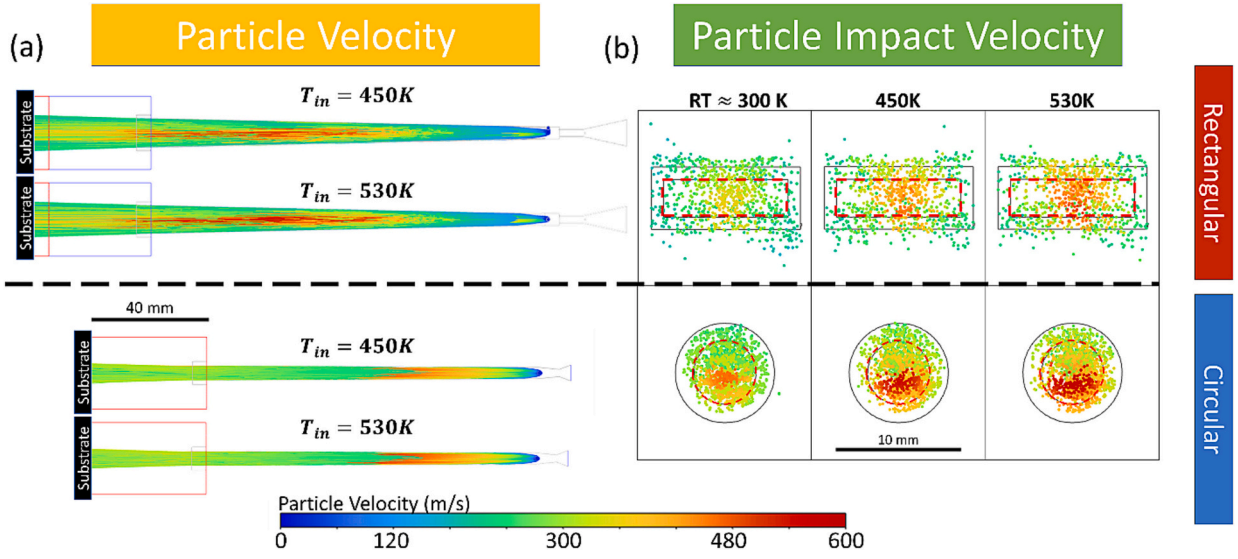


Fig. 7. Effects of the inlet gas temperature on (a) particle velocity development and (b) particle impact velocity.

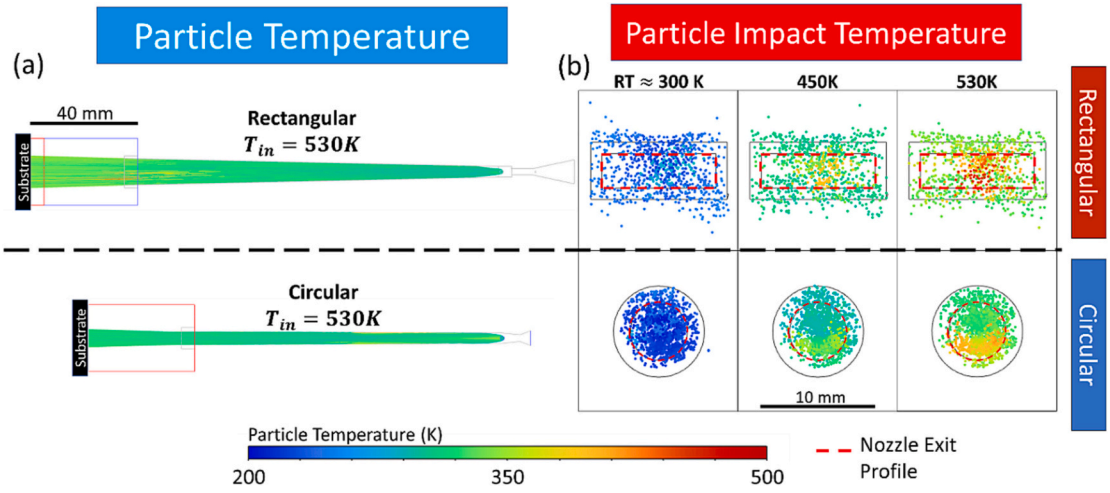


Fig. 8. Effects of nozzle inlet temperature on (a) Sn particle temperature development in the nozzle flow and (b) Sn particle impact temperature.

circular nozzle, which increases the relative overall powder temperature compared to the circular nozzle.

The powder impact temperatures, shown in Fig. 8b, show a clear picture of how the inlet temperature of the nozzle affects powder dispersion. When the inlet temperature is close to room temperature (300 K), the powders are cooled down due to the rapid expansion of the gas flow inside the nozzle. Comparing the powder impact temperatures at 450 K and 530 K, it was found that the average powder temperature in the rectangular nozzle is higher, with the highest temperatures located in the center of the rectangular nozzle. Additionally, the particles with the highest temperatures in the circular nozzle are located at the bottom of the nozzle profile. In both the rectangular and circular cases, the higher powder temperatures correspond to the higher powder velocities. It indicates that the powders exposed to the gas flow without energy dissipation achieve both high velocity and high temperatures. Notably, it was interestingly observed that the circular nozzle produced the highest impact velocity, whereas the rectangular nozzle generated the highest impact temperature.

4. Experimental section

A case study on cold spray metallization of a composite substrate was conducted to experimentally investigate the particle deposition characteristics raised by different nozzle profiles (i.e., circular and rectangular). Composite materials, such as GFRP and CFRP, are known for their significant strength-durability ratio, and therefore can be used in environments that are subject to extreme conditions, such as wind turbines and airplanes. Moreover, functional metallization on these important materials is of high interest as it enhances their surface hardness, wear resistance, tribological performance, and thermal/electrical conductivity [49–51]. Noteworthy, GFRP is a dielectric (i.e., insulator) material in contrast to CFRP [52], thereby making it a crucial application domain for CS metallization on this important substrate. As such, in this study, GFRP was intentionally selected as a substrate material, and subsequently metallized by the CS of Sn particles under the process settings listed in Table 2.

Table 2
CS settings used in experimental studies.

Working gas	Air
Gas inlet gauge pressure (MPa)	0.7
Gas inlet temperature (°C)	25 (RT) – 200
Powder flow rate (g·s^{-1})	0.3
Nozzle transverse speed (mm·s^{-1})	50
Nozzle stand-off distance (mm)	30

As for the feedstock coating material, Sn was selected due to its low critical velocity [2] in tandem with its low melting temperature. The low melting temperature allows particles to experience more significant thermal softening, thereby improving the deposition probability [2]. In addition, a single layer of Sn can provide electrically conductive coating, whereas hard particles such as Cu often require additional over-coating steps such as electroless or electroplating to create a conductive layer [8,53,54].

In the experimental studies, three different gas temperature settings in a range of 25–200 $^{\circ}C$ were considered to investigate the effect of gas temperature on particles' dispersion characteristics, as well as resulting deposition properties. After single-pass deposition on the specimens, each sample was evaluated by considering three different features, namely: i) coating (layer) thickness; ii) electrical resistance; and iii) surface roughness.

Fig. 9a–b shows the temperature distribution of the nozzle via thermal imaging taken by an IR camera (FLIR, A300). A lower outlet temperature was observed in the case of the rectangular nozzle as compared to the circular profile. Additionally, it was observed a non-uniform temperature profile along the divergent section of the rectangular nozzle while the circular nozzle has a more uniform temperature distribution. It is likely attributed to the construction of the rectangular nozzle that involves additional structural features, which increased the heat transfer surface area with the surrounding air, resulting in a lower and non-uniform measured temperature along the divergent section. Additionally, as seen in Fig. 9a–b, the maximum temperatures of the nozzle walls do not reach the measured outlet gas temperature as both nozzles dissipate some heat energy to the surroundings. This contextualizes the CFD results in Fig. 3c, where an error rate of 4.1 % was observed between simulated and experimental results. In other words, the numerical model does not consider heat convection and conduction from the nozzle walls, which could explain the error rate in numerical modeling results for this particular case.

Fig. 9c–d shows the effect of the gas temperature on resulting deposition in terms of electrical resistance, surface roughness, and layer thickness. Notably, even though the successful deposition was obtained at room temperature (RT) using the circular nozzle, no deposition was observed with the rectangular nozzle at RT. It is attributed to the lower impact velocity of particles under the rectangular nozzle flow, which could not exceed the critical velocity for achieving mechanical interlocking with the target substrate. The results from CFD simulations in Figs. 5–6 show that the majority of powders do not reach elevated impact velocities (>300 m/s) since the rectangular nozzle's early flow separation (see Fig. 4) does not allow the powders to accelerate through the entirety of the nozzle. On the other hand, the circular nozzle can

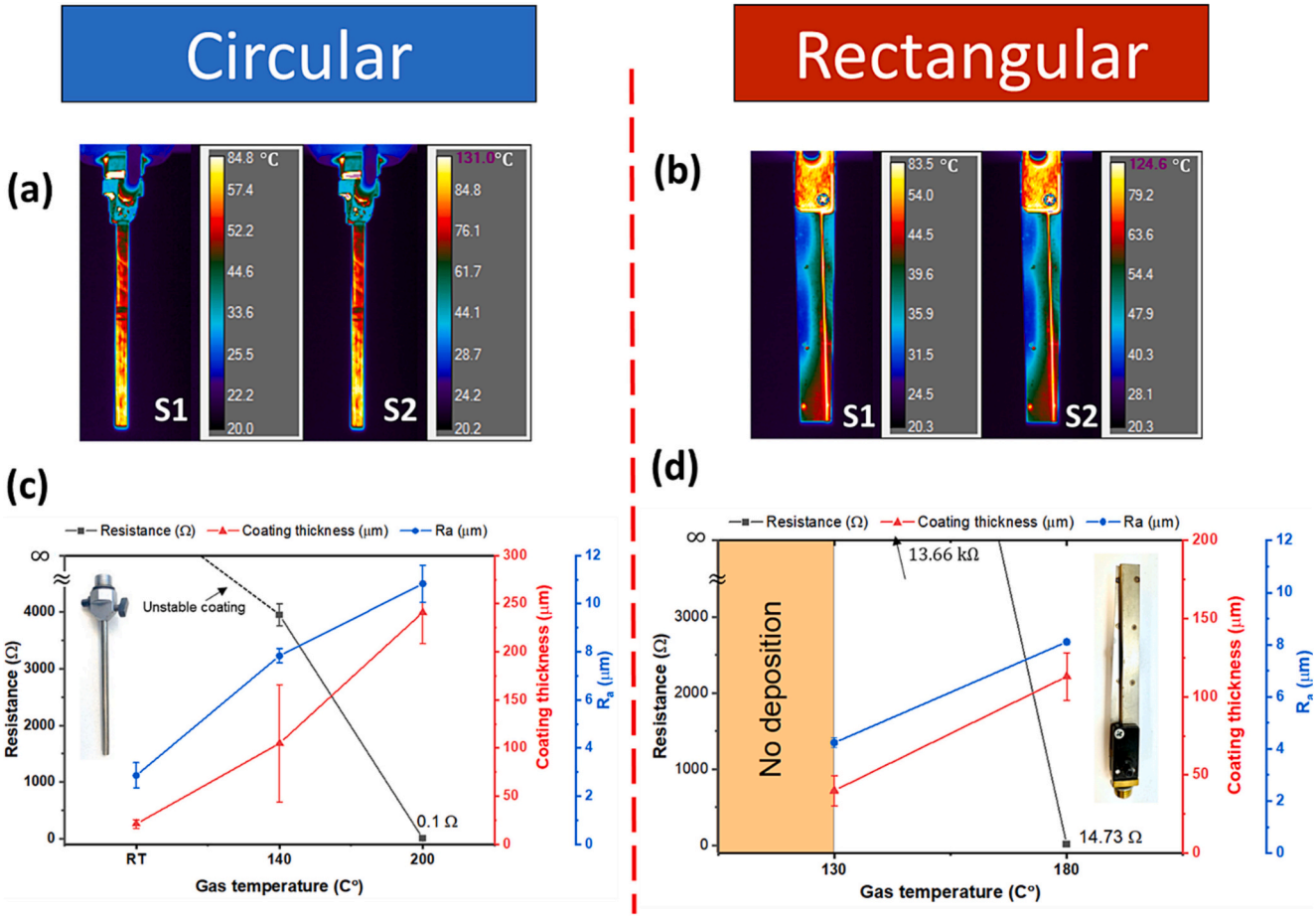


Fig. 9. Effect of gas temperature on temperature distribution of (a) circular nozzle and (b) rectangular nozzle; effect of gas temperature on coating thickness, surface roughness, and electrical resistance in case of (c) circular nozzle and (d) rectangular nozzle.

accelerate the powders to higher velocities than the rectangular profile.

Investigations into the surface roughness of the deposited lines in Fig. 9c–d showed a linear correlation between coating thickness and surface roughness. Additionally, the circular nozzle (Fig. 9c) produced coatings with larger average surface roughness, with $R_a = 7.83$ μm at $T = 140\ ^{\circ}C$ and $R_a = 10.83$ μm at $T = 200^{\circ}C$. Comparatively, the surface roughness was measured as $R_a = 4.24$ μm in case of rectangular nozzle at $T = 130^{\circ}C$ and $R_a = 8.11$ μm at $T = 180^{\circ}C$. These differences in surface roughness can be attributed to the rectangular nozzle's ability to disperse powders more evenly, resulting in a smoother deposition. The CFD simulation results in Fig. 7b confirm this phenomenon, where the spray pattern from the rectangular nozzle on the target substrate is more evenly distributed compared to the cluttered spray pattern of the circular nozzle. The results indicate that the rectangular nozzle can provide more uniform particle deposition on the target surface as compared to the circular nozzle.

As for the layer thickness, the circular nozzle led to an increased thickness at each CS setting as compared to the rectangular nozzle. The reason lies in the reduced particle velocity compared to the circular nozzle, which can be also seen from the numerical modeling results in Figs. 5 and 7b. Also, it was observed that there is a quasi-linear relationship between gas temperature and layer thickness. This statement is correct for both nozzle profiles. The larger average coating thickness of the circular nozzle can be attributed to its ability to accelerate the powders to higher velocities (Fig. 7b) compared to the rectangular nozzle at the same inlet temperatures, as more powders are able to reach critical velocity to deposit onto the GFRP. Overall, a maximum layer thickness of 214 μm was obtained by using the circular nozzle, while the rectangular nozzle led to a 104.8 μm thick layer, which is 51 % thinner than that of the circular nozzle case.

Analyzing the deposition samples in Fig. 10a shows that the deposited spray width is wider than the nozzle exit dimensions, which have widths of 5 mm for the circular nozzle and 10.35 mm for the rectangular nozzle (see Fig. 1c). Measuring the width of the powder dispersion at the simulated impact plane in Fig. 7b showed that the rectangular nozzle has a maximum spray width of 12.25 mm and the circular nozzle has a maximum spray width of 7 mm. The measured spray dimensions shown in Figs. 9c–d and 10a demonstrate that for the circular nozzle, $T_{outlet} = 140^{\circ}C$ results in a 6.8 mm wide line, and $T_{outlet} = 200^{\circ}C$ results in a deposited line with 5.6 mm wide. In addition, there is a 10 mm wide section of overspray resulting from stray powders, but is not considered a part of the main deposited line. The rectangular nozzles produced a coated linewidth of 11.4 mm at $T_{outlet} = 130^{\circ}C$, and a 12.4 mm wide coated line at $T_{outlet} = 180^{\circ}C$.

Calculating the percentage difference between the simulated powder spray widths in Figs. 7–8 to the deposited spray widths shows that the rectangular nozzle produced a 6.9 % thinner line at $T_{outlet} = 130^{\circ}C$ and a 1.2 % wider line at $T_{outlet} = 180^{\circ}C$. With the circular nozzle, a 2.8 % thinner line was produced at $T_{outlet} = 140^{\circ}C$ and a 20 % thinner line was produced at $T_{outlet} = 200^{\circ}C$ with overspray, which is 42 % thicker than the simulated spray width. The increase in spray width for the rectangular nozzle and the amount of overspray in the circular nozzle can be attributed to the increased temperature and velocity at higher gas temperatures, as seen in Figs. 7–8. However, the larger powder dispersion of the rectangular nozzle and increase in powder temperature correlate better with the increase in the rectangular nozzle's width.

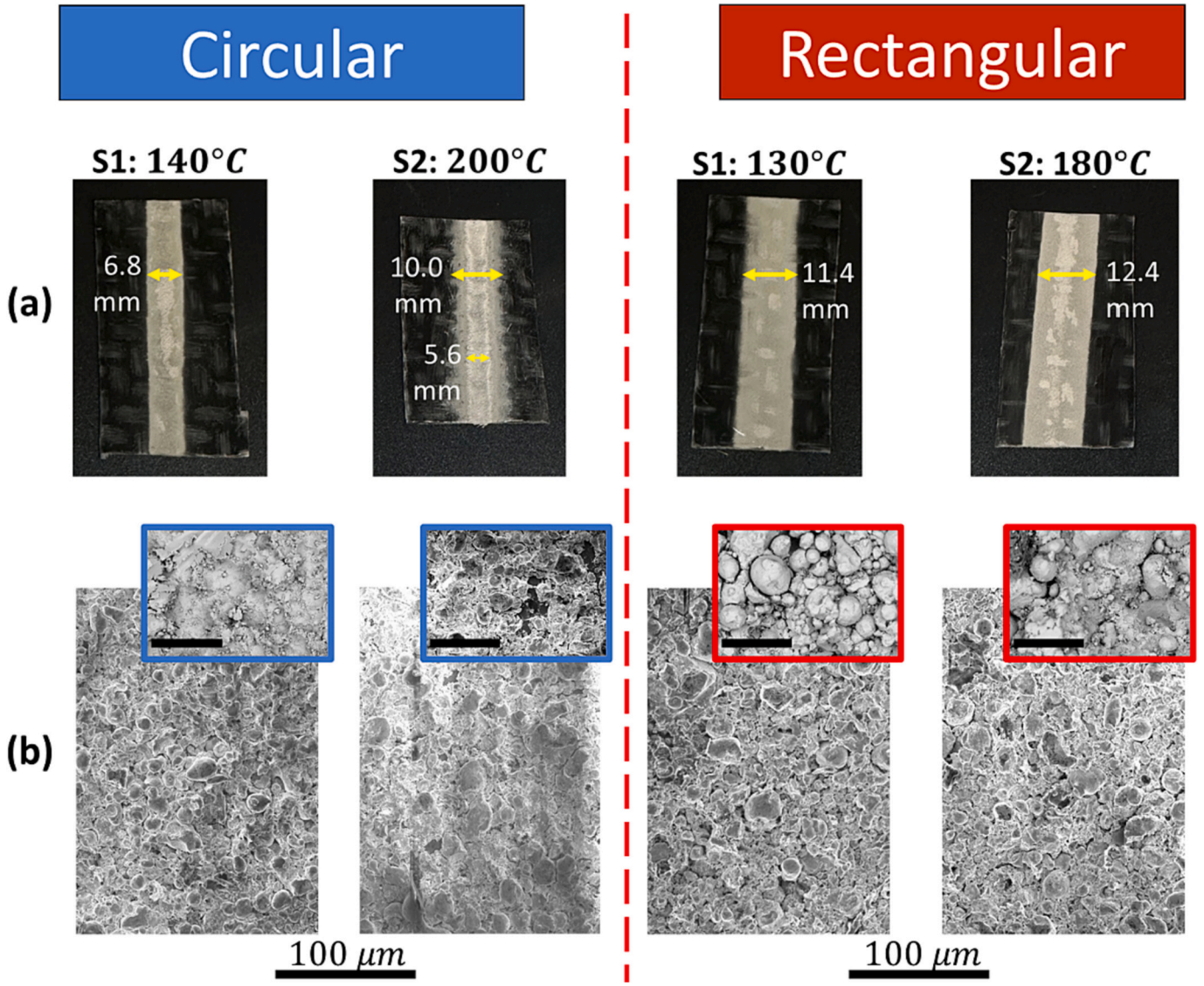


Fig. 10. **(a)** deposition samples with measured coating widths and **(b)** microstructure of deposited Sn layer with respect to nozzle geometry at various inlet temperatures; Scale of the enclosed SEM images = 50 μm.

Meanwhile, the circular nozzle does not disperse the powders as much, and a large portion of the powders within the circular nozzle's projected 5 mm exit diameter are accelerated to a much higher velocity compared to the powders outside this diameter, as seen in CFD simulations in Fig. 7b. This disparity results in a much smaller line width (with greater layer thickness) as the powders with the highest velocity produce the deposited line. Overall, the CFD simulations can predict powder spray width on GFRP samples within a 20 % error rate for the circular nozzle and a 7 % error rate for the rectangular nozzle.

Lastly, the electrical resistance of the resulting deposition was evaluated for both nozzle profiles. As shown in Fig. 9c–d, the deposition with the circular nozzle led to significantly lower electrical resistance (i.e., nearly 1–2 orders of magnitude) than that of the rectangular nozzle at similar gas temperatures. The reason can be attributed to the higher impact velocity of the circular nozzle (Fig. 7b), which increases coating layer thickness, and therefore decreases the measured Sn line resistance according to the electrical conductivity eq. ($R=\rho L/(wt)$), where R is the electrical resistance, ρ is the resistivity, L is the length, w is the width, and t is the layer thickness of the electrode. Additionally, elevated temperatures increase the powder temperatures (Fig. 8b), which facilitates the mechanical interlocking between the particles and the substrate [55], resulting in thicker layer thickness with lower electrical resistance (i.e., higher conductivity).

This can be elucidated further through the microstructural analyses shown in Fig. 10b, wherein elevated gas temperatures correspond to enhanced bonding between the powders. At higher outlet temperatures (180–200°C), powders exhibited fusion, indicating a consolidated deposition for both nozzle profiles. The combined effect of increased powder velocity and temperature generated a smooth deposited Sn layer, which resulted in the lowest measured resistance as 0.1 Ω for the circular nozzle and 14.3 Ω for the rectangular nozzle, respectively. Fig. 11 shows the electrical resistance variation of the resulting deposition at various gas temperatures produced by using both circular and rectangular nozzle profiles. To normalize the linewidth effects, the sheet resistance was also characterized in addition to the two-point probe results. The higher outlet temperatures (180–200°C), were measured to be on average 0.00997 Ω/□ for the circular nozzle and 83.5 Ω/□ for the rectangular nozzle, respectively. For the lower inlet temperatures, no homogeneous conductivity was observed. Overall, the results indicate that the circular nozzle is preferable over the rectangular nozzle to achieve higher electrically conductive functional coatings.

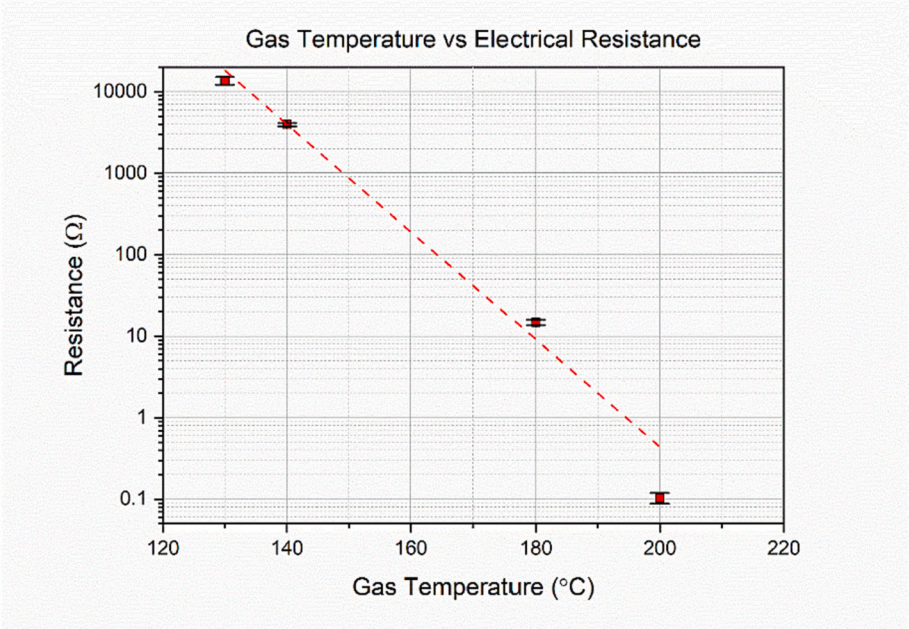


Fig. 11. Relationship between the gas temperature and electrical resistance of the Sn layer on the GFRP substrate.

5. Conclusion

In this study, the effect of axisymmetric (circular) and non-axisymmetric (rectangular) nozzle profiles on gas dynamics and powder flow structure in CS was studied through numerical modeling. A 3D Eulerian-Lagrangian turbulent scheme was employed to simulate the gas flow dynamics and particles dispersion behavior in both nozzle profiles. The effects of inlet gas pressure, temperature, and powder material on the gas-powder flow structure were then comprehensively investigated. Afterwards, an experimental case study on CS polymer metallization was performed using both rectangular and axisymmetric nozzles at varying inlet temperatures. The following results can be drawn from this study:

- The rectangular nozzle consistently experienced flow separation, characterized by oblique shock formation, across all tested inlet pressures (0.5–0.7 MPa) due to its non-axisymmetric geometry. In contrast, the circular nozzle showed a slightly overexpanded flow with minimal or no flow separation.
- Increasing the inlet gas pressure resulted in reduced powder dispersion on the target surface, with more significant effects for the rectangular nozzle as compared to the circular nozzle.
- The choice of powder material, specifically switching from Cu to Sn contributed to decreased powder spread due to the higher inertia and greater particle size (d_{50}) of the Cu particles compared to Sn powders. Also, smaller diameter powders were observed to be better focused by the gas flow, whereas larger diameter powders were dispersed more on the target substrate.
- Higher inlet gas temperatures led to elevated powder velocity and temperature for both nozzle types, consistent with the ideal gas law. However, the circular nozzle produced higher particle velocity, but lower particle impact temperature as compared to the rectangular nozzle. This trend is correct for all the inlet gas pressures and temperatures evaluated in this study.
- Increasing the inlet temperature from 450 K to 530 K resulted in a wider deposited line (8.8 %) for the rectangular nozzle.
- The rectangular nozzle created a more uniform deposition (R_a = 8.12 μm) compared to the circular nozzle (R_a = 10.83) at the same CS process settings.
- Deposition experiments conducted on a GFRP substrate revealed that the rectangular nozzle produces a 53 % thinner deposited layer (film) thickness compared to the circular nozzle.
- CS metallization on the GFRP target using the circular nozzle led to significantly lower electrical resistance (143-fold) compared to that of rectangular nozzle under the same CS conditions.
- Overall, the numerical simulations along with the experimental case study demonstrated that the rectangular nozzle profile leads to more uniform particle deposition with wider line resolution in CS as compared to the circular nozzle. However, the circular nozzle is more preferable to achieve thicker layer deposition with greater electrical conductivity (less resistance) over the rectangular nozzle.

Future directions may focus on the evaluation of rectangular and circular nozzle profiles under high-pressure CS conditions, as the development of gas and powder flow is anticipated to differ under these conditions. Furthermore, studies that focus on multi-layer and multi-material deposition on composite materials can pave the way for expanding the application domain of the emerging CS technology.

CRediT authorship contribution statement

Theodore Gabor: Conceptualization, formal analysis, design, investigation, experiments, characterization, visualization, data curation, writing original draft.

Semih Akin: Conceptualization, design, characterization, writing original draft, review & editing.

Martin Byung-Guk Jun: Conceptualization, supervision, resources, review & editing.

Declaration of competing interest

The authors declare no competing interests.

Appendix A. Supplementary data

Supplementary data to this article can be found online at https://doi.org/10.1016/j.jmapro.2024.02.005.

References

[1] Irissou E, Legoux JG, Ryabinin AN, Jodoin B, Moreau C. Review on cold spray process and technology: part I-intellectual property. Journal of Thermal Spray Technology 2008;17:495–516. https://doi.org/10.1007/s11666-008-9203-3.

[2] Klassen T, Gärtner F, Schmidt T, Kliemann JO, Onizawa K, Donner KR, et al. Basic principles and application potentials of cold gas spraying. Materwiss Werksttechvol. 41. John Wiley & Sons, Ltd; 2010. p. 575–84. https://doi.org/10.1002/mawe.201000645.

[3] Yin S, Cavaliere P, Aldwell B, Jenkins R, Liao H, Li W, et al. Cold spray additive manufacturing and repair: fundamentals and applications. Addit Manuf 2018;21:628–50. https://doi.org/10.1016/J.ADDMA.2018.04.017.

[4] Raoelison RN, Xie Y, Sapanathan T, Planche MP, Kromer R, Costil S, et al. Cold gas dynamic spray technology: a comprehensive review of processing conditions for various technological developments till to date. Addit Manuf 2018;19:134–59. https://doi.org/10.1016/J.ADDMA.2017.07.001.

[5] Moridi A, Hassani-Gangaraj SM, Guagliano M, Dao M. Cold spray coating: review of material systems and future perspectives. Surf Eng 2014;30:369–95. https://doi.org/10.1179/1743294414Y.0000000270.

[6] Champagne VK. Repair of magnesium components by cold spray techniques. The Cold Spray Materials Deposition Process: Fundamentals and Applications 2007:327–52. https://doi.org/10.1533/9781845693787.3.327.

[7] Champagne V, Helfritch D. The unique abilities of cold spray deposition FULL CRITICAL REVIEW the unique abilities of cold spray deposition. Int Mater Rev 2016:61. https://doi.org/10.1080/09506608.2016.1194948.

[8] Akin S, Tsai JT, Park MS, Jeong YH, Jun MBG. Fabrication of electrically conductive patterns on acrylonitrile-butadiene-styrene polymer using low-pressure cold spray and electroless plating. J Micro Nanomanuf 2020:8. https://doi.org/10.1115/1.4049578/1096356.

[9] Tsai J-T, Akin S, Zhou F, Park MS, Bahr DF, Jun MB-G. Electrically conductive metallized polymers by cold spray and co-electroless deposition. ASME open. Journal of Engineering 2022:1. https://doi.org/10.1115/1.4053781.

[10] Della Gatta R, Perna AS, Viscusi A, Pasquino G, Astarita A. Cold spray deposition of metallic coatings on polymers: a review. J Mater Sci 2022;57:27–57. https://doi.org/10.1007/s10853-021-06561-2.

[11] Amin S, Panchal H. A review on thermal spray coating processes. International Journal of Current Trends in Engineering & Research (IJCTER) 2016;2:556–63.

[12] Akin S, Nath C, Jun MB-G. Selective surface metallization of 3D-printed polymers by cold-spray-assisted electroless deposition. ACS Appl Electron Mater 2023. https://doi.org/10.1021/acsaelm.3c00893.

[13] Lupoi R, O'Neill W. Deposition of metallic coatings on polymer surfaces using cold spray. Surf Coat Technol 2010;205:2167–73. https://doi.org/10.1016/J.SURFCOAT.2010.08.128.

[14] Melentiev R, Yu N, Lubineau G. Polymer metallization via cold spray additive manufacturing: a review of process control, coating qualities, and prospective applications. Addit Manuf 2021;48:102459. https://doi.org/10.1016/J.ADDMA.2021.102459.

[15] Pathak S, Saha GC. Development of sustainable cold spray coatings and 3D additive manufacturing components for repair/manufacturing applications: a critical review. Coatings 2017;7:122. https://doi.org/10.3390/coatings7080122.

[16] Prashar G, Vasudev H. A comprehensive review on sustainable cold spray additive manufacturing: state of the art, challenges and future challenges. J Clean Prod 2021;310:127606. https://doi.org/10.1016/j.jclepro.2021.127606.

[17] Papyrin A. The development of the cold spray process. Woodhead Publishing Limited; 2007. https://doi.org/10.1533/9781845693787.1.11.

[18] Zucrow MJ, Hoffman JD. Gas dynamicsVol. I. New York: John Wiley and Sons Inc.; 1976. https://doi.org/10.1201/9781315274065-11.

[19] Zavalan F-L, Rona A. A workflow for designing contoured axisymmetric nozzles for enhancing additively manufactured cold spray deposits. Addit Manuf 2023;62:103379. https://doi.org/10.1016/j.addma.2022.103379.

[20] Suo XK, Liu TK, Li WY, Suo QL, Planche MP, Liao HL. Numerical study on the effect of nozzle dimension on particle distribution in cold spraying. Surf Coat Technol 2013;220:107–11. https://doi.org/10.1016/j.surfcoat.2012.09.029.

[21] Cao C, Han T, Xu Y, Li W, Yang X, Hu K. The associated effect of powder carrier gas and powder characteristics on the optimal design of the cold spray nozzle. Surf Eng 2020;36:1081–9. https://doi.org/10.1080/02670844.2020.1744297.

[22] Cao C, Li W, Zhang Z, Yang X, Xu Y. Cold spray additive manufacturing of Ti6Al4V: special nozzle design using numerical simulation and experimental validation. Coatings 2022;12:210. https://doi.org/10.3390/coatings12020210.

[23] Akin S, Wu P, Nath C, Chen J, Jun MB-G. A study on converging-diverging nozzle design for supersonic spraying of liquid droplets toward nanocoating applications. J Manuf Sci Eng 2023:145. https://doi.org/10.1115/1.4062351.

[24] Lupoi R, O'Neill W. Powder stream characteristics in cold spray nozzles. Surf Coat Technol 2011;206:1069–76. https://doi.org/10.1016/j.surfcoat.2011.07.061.

[25] Sova A, Grigoriev S, Kochetkova A, Smurov I. Influence of powder injection point position on efficiency of powder preheating in cold spray: numerical study. Surf Coat Technol 2014;242:226–31. https://doi.org/10.1016/j.surfcoat.2013.10.078.

[26] Huang G, Gu D, Li X, Xing L, Wang H. Numerical simulation on syphonage effect of laval nozzle for low pressure cold spray system. J Mater Process Technol 2014;214:2497–504. https://doi.org/10.1016/j.jmatprotec.2014.05.014.

[27] Garmeh S, Jadidi M, Dolatabadi A. Three-dimensional modeling of cold spray for additive manufacturing. Journal of Thermal Spray Technology 2020;29:38–50. https://doi.org/10.1007/s11666-019-00928-3.

[28] Garmeh S, Jadidi M, Lamarre J-M, Dolatabadi A. Cold spray gas flow dynamics for on and off-axis nozzle/substrate hole geometries. Journal of Thermal Spray Technology 2023;32:208–25. https://doi.org/10.1007/s11666-022-01487-w.

[29] Harihara Sudhan K, Krishna Prasad G, Kothurkar NK, Srikrishnan AR. Studies on supersonic cold spray deposition of microparticles using a bell-type nozzle. Surf Coat Technol 2020;383:125244. https://doi.org/10.1016/j.surfcoat.2019.125244.

[30] Alkhimov AP, Kosarev VF, Klinkov SV. The features of cold spray nozzle design. Journal of Thermal Spray Technology 2001;10(2):375–81. https://doi.org/10.1361/105996301770349466.

[31] Gabor T, Akin S, Tsai J-T, Jo S, Al-Najjar F, Jun MB-G. Numerical studies on cold spray particle deposition using a rectangular nozzle. In: Additive manufacturing; biomanufacturing; life cycle engineering; manufacturing equipment and automation; nano/micro/meso manufacturing. Vol. 1. American Society of Mechanical Engineers; 2022. https://doi.org/10.1115/MSEC2022-85673.

[32] Yin S, Fang Wang X, Ya Li W. Computational analysis of the effect of nozzle cross-section shape on gas flow and particle acceleration in cold spraying. Surf Coat Technol 2011;205:2970–7. https://doi.org/10.1016/j.surfcoat.2010.11.002.

[33] Akin S, Wu P, Tsai JT, Nath C, Chen J, Jun MBG. A study on droplets dispersion and deposition characteristics under supersonic spray flow for nanomaterial coating applications. Surf Coat Technol 2021;426:127788. https://doi.org/10.1016/J.SURFCOAT.2021.127788.

[34] Lee MW, Park JJ, Kim DY, Yoon SS, Kim HY, Kim DH, et al. Optimization of supersonic nozzle flow for titanium dioxide thin-film coating by aerosol deposition. J Aerosol Sci 2011;42:771–80. https://doi.org/10.1016/J.JAEROSCI.2011.07.006.

[35] Varadaraajan V, Mohanty P. Design and optimization of rectangular cold spray nozzle: radial injection angle, expansion ratio and traverse speed. Surf Coat Technol 2017;316:246–54. https://doi.org/10.1016/j.surfcoat.2017.03.005.

[36] Yin S, Meyer M, Li W, Liao H, Lupoi R. Gas flow, particle acceleration, and heat transfer in cold spray: a review. Journal of Thermal Spray Technology 2016;25:874–96. https://doi.org/10.1007/s11666-016-0406-8.

[37] Kowalski K, Błasiak P, Pietrowicz S. A novel cold spray process flow technique - a numerical investigation. Int J Heat Mass Transf 2024;218:124817. https://doi.org/10.1016/J.IJHEATMASSTRANSFER.2023.124817.

[38] Özdemir OÇ, Conahan JM, Müftü S. Particle velocimetry, CFD, and the role of particle sphericity in cold spray. Coatings 2020;10:1254. https://doi.org/10.3390/coatings10121254.

[39] Fluent Thoery Guide. Ansys fluent theory guide. ANSYS Inc, USA 2013;15317:724–46.

[40] Shih T-H, Liou WW, Shabbir A, Yang Z, Zhu J. A new k-ϵ eddy viscosity model for high reynolds number turbulent flows. Compurers Fluids 1995;24:227–38.

[41] Morsi SA, Alexander AJ. An investigation of particle trajectories in two-phase flow systems. J Fluid Mech 1972;55:193–208. https://doi.org/10.1017/S0022112072001806.

[42] Jen TC, Li L, Cui W, Chen Q, Zhang X. Numerical investigations on cold gas dynamic spray process with nano- and microsize particles. Int J Heat Mass Transf 2005;48:4384–96. https://doi.org/10.1016/j.ijheatmasstransfer.2005.05.008.

[43] Rosin P, Rammler E. The laws governing the fineness of powdered coal. Journal of the Institute of Fuel 1933;7:29–36.

[44] Akin S, Wu P, Tsai JT, Nath C, Chen J, Jun MBG. A study on droplets dispersion and deposition characteristics under supersonic spray flow for nanomaterial coating applications. Surf Coat Technol 2021;426:127788. https://doi.org/10.1016/J.SURFCOAT.2021.127788.

[45] Singhal C, Murtaza Q. Simulation of critical velocity of cold spray process with different turbulence models. Mater Today Proc 2018;5:17371–9.

[46] Garmeh S, Jadidi M, Dolatabadi A. Three-dimensional modeling of cold spray for additive manufacturing. Journal of Thermal Spray Technology 2020;29:38–50. https://doi.org/10.1007/s11666-019-00928-3.

[47] Haghbin N, Khakpour A, Schwartzentruber J, Papini M. Measurement of abrasive particle velocity and size distribution in high pressure abrasive slurry and water micro-jets using a modified dual disc anemometer. J Mater Process Technol 2019;263:164–75. https://doi.org/10.1016/J.JMATPROTEC.2018.08.014.

[48] Tsai JT, Akin S, Zhou F, Bahr DF, Jun MBG. Establishing a cold spray particle deposition window on polymer substrate. Journal of Thermal Spray Technology 2021;30:1069–80. https://doi.org/10.1007/S11666-021-01179-X/FIGURES/13.

[49] Perna AS, Viscusi A, Astarita A, Boccarusso L, Carrino L, Durante M, et al. Manufacturing of a metal matrix composite coating on a polymer matrix composite through cold gas dynamic spray technique. J Mater Eng Perform 2019;28:3211–9. https://doi.org/10.1007/s11665-019-03914-6.

[50] Astarita A, Boccarusso L, Durante M, Viscusi A, Sansone R, Carrino L. Study of the production of a metallic coating on natural fiber composite through the cold spray technique. J Mater Eng Perform 2018;27:739–50. https://doi.org/10.1007/s11665-018-3147-7.

[51] Rubino F, Tucci F, Esperto V, Perna AS, Astarita A, Carlone P, et al. Metallization of Fiber reinforced composite by surface functionalization and cold spray deposition. Procedia Manuf 2020;47:1084–8. https://doi.org/10.1016/j.promfg.2020.04.353.

[52] Jahangiri T, Wang Q, Faria Da Silva F, Leth Bak C. Lecture notes in electrical engineering 557 electrical design of a 400 kV composite tower n.d.

[53] Fallah P, Rajagopalan S, McDonald A, Yue S. Development of hybrid metallic coatings on carbon fiber-reinforced polymers (CFRPs) by cold spray deposition of copper-assisted copper electroplating process. Surf Coat Technol 2020;400:126231. https://doi.org/10.1016/j.surfcoat.2020.126231.

[54] Akin S, Nath C, Jun MB-G. Selective surface metallization of 3D-printed polymers by cold-spray-assisted electroless deposition. ACS Appl Electron Mater 2023. https://doi.org/10.1021/acsaelm.3c00893.

[55] Viscusi A, Astarita A, Della Gatta R, Rubino F. A perspective review on the bonding mechanisms in cold gas dynamic spray. Surf Eng 2019;35:743–71. https://doi.org/10.1080/02670844.2018.1551768.